Fast LV Motion Estimation Using Subspace Approximation Techniques

Yu-Ping Wang, *Member, IEEE*, Yasheng Chen, and Amir A. Amini*, *Senior Member, IEEE*

***Abstract*—Cardiac motion estimation is very important in understanding cardiac dynamics and in noninvasive diagnosis of heart disease. Magnetic resonance (MR) imaging tagging is a technique for measuring heart deformations. In cardiac tagged MR images, a set of dark lines are noninvasively encoded within myocardial tissue providing the means for measurement of deformations of the heart. The points along tag lines measured in different frames and in different directions carry important information for determining the three-dimensional nonrigid movement of left ventricle. However, these measurements are sparse and, therefore, multidimensional interpolation techniques are needed to reconstruct a dense displacement field. In this paper, a novel subspace approximation technique is used to accomplish this task. We formulate the displacement estimation as a variational problem and then project the solution into spline subspaces. Efficient numerical methods are derived by taking advantages of B-spline properties. The proposed technique significantly improves our previous results reported in [3] with respect to computational time. The method is applied to a temporal sequence of two-dimensional images and is validated with simulated and *in vivo* heart data.**

***Index Terms*—Deformable models, motion analysis, splines, variational methods, vector field reconstruction.**

I. Introduction

A. Tagged Magnetic Resonance (MR): Imaging

ONE of the promising techniques for noninvasive study of left-ventricular (LV) wall motion is tagged magnetic resonance (MR) imaging. It provides a tool for assessing the dynamic motion or deformation of the human heart, which is invaluable in the diagnosis of heart disease.

MRI is a noninvasive imaging technique that provides superb anatomic information with excellent spatial resolution and soft-tissue contrast. Conventional MR studies of the heart provide accurate measures of global myocardial function, chamber volumes and ejection fractions, and regional wall motions and thickening. The principle of MR tagging is based on altering the magnetization property of selective material points in the myocardium in order to create tagged patterns within a deforming body such as the heart muscle. The resulting pattern defines a time-varying curvilinear coordinate system on the tissue. During tissue contractions, the grid patterns move, allowing for visual tracking of the grid intersections over time. The intrinsic high spatial and temporal resolutions of such myocardial analysis schemes provide unsurpassed information about local contraction and deformation in the heart wall, which can be used to derive local strain and deformation indices from different myocardial regions.

Several techniques for acquiring tagged images for the analysis of time-varying motion of the LV have been reported in recent years. Spatial modulation of magnetization (SPAMM) [6] is a technique for producing a regular grid pattern in the imaging plane, introduced by Axel and Dougherty. This method uses a binomial pulse to produce spatial modulation of spins in the tissue which results in a grid pattern on the image of the moving tissue. Hence, we only have a sparse set of displacement measurements at discrete points in space and time. This leads to the requirement for the computation of a dense displacement field from these sparse measurements.

B. Tagged MR: Image Analysis

Analysis of tagged MR images requires several image processing steps, such as automatic detection of tag line locations, epicardial and endocardial contour extraction, and finally cardiac motion estimation. In [24], an analysis system based on snakes was adopted. The stripe displacements were fitted by a three-dimensional (3-D) finite-element model (FEM). Although the FEM model provides good local strain analysis, it results in a large number of model parameters. The work described in [16] considers geometric primitives which are generalization of volumetric ellipsoids. Use of parameter functions in this context allows for spatial variations of aspect ratios of the model to fit the LV. The models are also further generalized to parameterize twisting motion about the long axis of the LV as a function of distance along the long axis as well as the radial direction.

Methods based on optical flow have also been applied to the analysis of tagged MR images. An approach called variable brightness optical flow (VBOF) accounts for temporal variation of signal intensities. The algorithm described in [11] relaxes the intensity constancy constraint and allows for intensity variations to be modeled by a more accurate local linear transformation.

In [15], the authors perform least squares fitting of a truncated power series in the prolate spheroidal coordinate system on the whole of the myocardium in order to measure dense displacements. One difficulty with this approach is that the interpolation is not local. An alternate approach to motion reconstruction developed in [9] utilizes a multidimensional stochastic model for the true displacement field and the Fisher estimation framework

Manuscript received April 3, 2000; revised March 20, 2001. This work was supported by the National Institutes of Health (NIH) under Grant HL-57628 and Grant HL 64217 and by the National Science Foundation (NSF) under Grant IRI-9796207. The Associate Editor responsible for coordinating the review of this paper and recommending its publication was M. Unser. *Asterisk indicates corresponding author.*

Y.-P. Wang is with The Advanced Digital Imaging Research, LLC., League City, TX 77573 USA.

Y. Chen is with the CVIA Laboratory, Washington University Medical Center, St. Louis, MO 63130 USA.

*A. A. Amini is with the CVIA Laboratory, Box 8086, 660 S. Euclid Avenue, Washington University Medical Center, St. Louis, MO 63130 USA (e-mail: amini@cauchy.wustl.edu).

Publisher Item Identifier S 0278-0062(01)04689-4.

to estimate displacement vectors in points on the lattice. The advantage of this framework is an error covariance which determines the number of tag lines needed to achieve a given estimation accuracy.

In [12], a four-dimensional time-varying B-spline model is fitted to generate a B-solid which varies continuously over time t. One important advantage of the model is that 3-D material point localization and 3-D displacement reconstruction are achieved simultaneously at any time instant in a single step. The displacements are obtained by taking the difference of fitted B-solids between two frames. In [17], a volumetric B-solid model was proposed to concurrently track tag lines in different image slices by implicitly defined B-surfaces which align themselves with tagged points. The solid is a 3-D tensor product B-spline whose isoparametric curves deform under image forces from tag lines in different image slices.

In [1] and [2], tag lines are tracked with dynamic programming B-snakes and B-snake grids. In [1], a constrained thin-plate spline reconstruction of the displacement field was proposed from points and lines based on a variational formulation. In [3], an optimization method was proposed which improved on the reconstruction technique in [1]. One advantage of the approach proposed in [3] is that it allows for reconstruction of dense deformations between two arbitrary frames in a sequence of tagged images, as motion reconstruction methods generally produce displacement vector fields relative to undeformed tags in the initial frame. In the present paper, we develop an efficient numerical method which results in about a 1-min computation time on a Sun Workstation for reconstructing the motion field between two frames. Moreover, high accuracy is achieved at the same time. The displacement vector field at any time frame is reconstructed with respect to frame zero, and the displacement field between two arbitrary frames is obtained by simply taking the difference between them.

The organization of the paper is as follows. Section II presents a continuous model formulating the estimation of heart wall deformation. Section III presents definitions and properties of B-splines, which are useful in the derivation of the numerical algorithm. Following this section, we derive efficient algorithms for reconstruction of dense displacement fields. The techniques adopt spline approximations in finite-dimensional subspaces. In particular, the computation of the values of B-splines at integers will be given in detail. The validations of the reconstruction methods both with the simulated data and *in vivo* data are given in Section V.

II. Continuous Formulation of the Model for Tagged MRI Motion Estimation

Tracking tissue deformations with SPAMM using coupled B-snake grids provides two-dimensional (2-D) displacement information at tag intersections and one-dimensional (1-D) displacement information along other 1-D snake points [1], [3]. The displacement measurement from tag lines, however, are sparse; interpolation is required to reconstruct a dense displacement field from which strain, torsion, and other mechanical indices of function can be computed at all myocardial points. This is illustrated as in Fig. 1. In this section, we describe an efficient solution to the formulation in [1] and [3]. The algorithm improves on previous methods in both the computation time and the accuracy for reconstructing a dense displacement vector field using localized coordinates of tag positions. In this development, we assume only 2-D motion (as is roughly the case toward the apical end of the heart [18]). The extension to 3-D case will be developed in another paper.

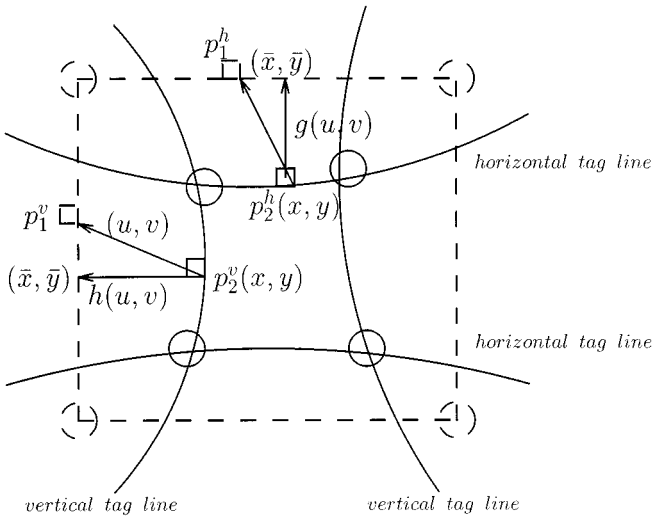

Fig. 1. A deformed tag line (in solid line) and its corresponding undeformed tag line (in dotted line). The intersections or landmark points are denoted as circles. From these intersections we know both the x and y components of the displacements. But for other tag points p_2^h along the horizontal and P_2^v along the vertical lines, as indicated by the squares, we only know their y and x components of the displacements, $g(u,v)$ and $h(u,v)$, respectively. We want to make use of all these available information to estimate the dense displacement field.

The intersections of two grids are "pulled" toward one another by minimizing

$$\Phi_1 = \sum_N (u - u^{\text{int}})^2 + (v - v^{\text{int}})^2 \tag{1}$$

where u and v are the x and y components of displacement vector field at a certain time frame relative to the initial undeformed frame. u^{int} and v^{int} are the x and y components of displacement at tag intersections as well as intersections of myocardial contours with tag lines. The summation in (1) is over all the N tag intersection points. This form of the intersection spring constraint has also been used in a similar spirit in [24].

Assuming 2-D tissue motion, a further physical constraint is necessary: any point on a deformed tag in frame n must be warped to lie on its corresponding undeformed tag in frame 0 of the sequence. As described in [4], for a vector field to perform such a warp, $h(u,v)$ and $g(u,v)$ of Fig. 1 must be minimized. Let $P_2 = (x,y)$ be any point on the deformed tag line, and $P_1(u,v) = (x,y)+(u,v)$ be the corresponding point in the undeformed frame as in Fig. 1. The following term is then summed over all deformed horizontal and vertical grid points:

$$\begin{aligned}\Phi_2 &= \sum_{N_y} h(u,v)^2 + \sum_{N_x} g(u,v)^2 \\ &= \sum_{N_y} ((P_1(u,v) - P_2)\cdot n_x)^2 \\ &\quad + \sum_{N_x} ((P_1(u,v) - P_2)\cdot n_y)^2 \\ &= \sum_{N_y} (x + u - \bar{x})^2 + \sum_{N_x} (y + v - \bar{y})^2 \end{aligned} \tag{2}$$

where n_x and n_y are the normal direction along x and y, respectively. In the above equation, (x, y) are the coordinates of a point on the tag line in the current frame, and $(\bar{x}, \bar{y})$ is the closest point to $(x+u, y+v)$ on the corresponding tag line in the undeformed frame. The quantities $h(u, v)$ and $g(u, v)$ are the horizontal and vertical distance from the point (x, y) to the undeformed vertical and horizontal tag line, respectively. Therefore, points on a deformed vertical tag line can be warped back to lie its corresponding undeformed vertical tag line, following minimization of $\sum(h(u,v))^2$. Similarly, minimization of $\sum(g(u,v))^2$ will result in warping points on deformed horizontal tag lines to horizontal tag lines in frame 0. The summation is over all the vertical tag number N_y and horizontal tag number N_x, respectively. Notice the difference between above formulation (which was proposed in [4]) and that of [3]. In [3], it is assumed that $(\bar{x}, \bar{y})$ is dependent on the vector field (u, v) and is computed from a nonlinear distance function with local minima, but here we only consider that $(\bar{x}, \bar{y})$ which lies on an undeformed tag line. Therefore, the above energy functional is quadratic in nature, having a unique global minimum.

The vector field continuity constraint is the bending energy of a thin-plate which is applied to the x and y component of the displacement field $(u(x, y), v(x, y))$

$$\Phi_3 = \int\int u_{xx}^2 + 2u_{xy}^2 + u_{yy}^2 dxdy + \int\int v_{xx}^2 + 2v_{xy}^2 + v_{yy}^2 dxdy \tag{3}$$

which serves as the smoothness constraint on the reconstructed vector field, characterizing approximating thin-plate splines.

An optimization function can be obtained by a linear combination of the three terms in (1)–(3). The objective function is

$$\Phi = \lambda_1\Phi_1 + \lambda_2\Phi_2 + \lambda_3\Phi_3. \tag{4}$$

The characterization of the solution to this variational problem is described in [20], which is treated as optimization problem in a reproducing kernel Hilbert space. The interpolation given specified landmarks is characterized by the thin-plate splines as investigated by Bookstein [8]. However, it is hard to get the explicit form of the solution to this general problem. It should be noted that essentially the same accuracy can be obtained in a computationally simpler way by minimizing (4) in a certain finite-dimensional approximating subspace. We chose such a subspace as that spanned by the shifted B-spline bases. In other words, the vector field is represented as a linear combination of shifted B-spline bases

$$\mathbf{U} = \sum_{i=1}^{M_x}\sum_{j=1}^{M_y} \mathbf{C}_{ij}\beta_{ij}^n(x, y), \quad \beta_{ij}^n(x, y) = \beta_i^n(x)\beta_j^n(y) \tag{5}$$

where

$\mathbf{U} = (u, v)^{\mathrm{T}}$ vector field;
$\mathbf{C} = (c, d)^{\mathrm{T}}$ control points or coefficients;
M_x, M_y size of the grid set by the user.

Larger values for M_x and M_y will result in higher computational costs. In the experiments, we set the size to 256×256. Since we assume knowing locations of the epicardial and endocardial contour, only the displacement vectors in the region between them will be computed. $\beta_i(x) = \beta(x - i)$, $(i \in Z)$ is the shifted B-splines, as will be defined below. Because the linear combinations of these shifted B-spline bases constitute a complete and stable approximation of $L^2(R)$ [23], the representation in (5) is reasonable. In the next section we will describe how to get an efficient numerical solution by using this subspace approximation approach.

III. B-Spline Basics

A. Definitions and Notations

We follow the convention of [22], [23] and define the continuous or analytic B-spline of order n by $\beta^n(x)$, which can be generated by repeated $n+1$ convolution of a B-spline of order zero

$$\beta^n(x) = \beta^0 * \beta^{n-1}(x) = \overbrace{\beta^0 * \beta^0 * \cdots \beta^0}^{n+1}(x) \tag{6}$$

where the zeroth-order B-spline $\beta^0(x)$ is the pulse function with support $[0, 1]$. The definition is a little different from that of [19] where the center of symmetry is at the origin. An alternative definition of these normalized B-spline functions is given by

$$\beta^n(x) = \sum_{j=0}^{n+1} \binom{n+1}{j} \frac{(-1)^j}{n!}(x-j)^n \mu(x-j) \tag{7}$$

where $\mu(x)$ is the step function

$$\mu(x) = \begin{cases} 1, & \text{for } x > 0 \\ 0, & \text{for } x < 0 \end{cases}$$

and where $\binom{n+1}{j}$ are the binomial coefficients.

The discrete sampled B-spline $b^n(k)$ of order n is obtained by directly sampling the nth-order continuous B-spline

$$b^n(k) = \beta^n(k) \quad \forall k \in Z. \tag{8}$$

The continuous convolution of functions f and g is defined as

$$f * g(x) = \int f(x-t)g(t)dt, \quad x \in R. \tag{9}$$

The discrete convolution between two sequences $\{a\}$ and $\{b\}$ is the sequence $\{a * b\}$

$$b * a(k) = \sum_{l=-\infty}^{\infty} b_{k-l}a_l. \tag{10}$$

The above definition of 1-D B-splines can be easily extended to the 2-D case through the tensor product.

B. Some Properties

B-spline bases enjoy many useful properties, which make them widely used in computer graphics and computer aided geometric design. For example, its local compact support and smoothness make them very suitable for surface and solid representation [3], [12], [13], [17]. In this section, we only present the properties used in the paper. Some additional details on properties of B-splines could be found in [14], [19], [22], and [23].

- The shifted B-spline bases constitute a stable and complete approximation of a square integrable function [22].
- The local support and symmetry of B-splines. The B-spline basis $\beta^n(x)$ has compact support $[0, n+1]$ and is symmetric with respect to the midpoint $(n+1)/2$, i.e.,

$$\beta^n(n+1-x) = \beta^n(x). \tag{11}$$

- The derivative of B-splines. If a curve is represented as B-spline segments, one can increase the smoothness by increasing the order of B-splines. The derivative of the nth order of B-splines is the difference of lower order B-splines. For example, the first and second-order derivatives of B-splines are

$$\begin{aligned}(\beta^n)'(x) =&\beta^{n-1}(x) - \beta^{n-1}(x-1),\\ (\beta^n)''(x) =&\beta^{n-2}(x) - 2\beta^{n-2}(x-1) + \beta^{n-2}(x-2).\end{aligned} \tag{12}$$

- The convolutions of two B-spline bases are still B-splines

$$\beta^n(x-l) * \beta^m(x-k) = \beta^{n+m-1}(x-k+l). \tag{13}$$

IV. Numerical Solutions Using Spline Subspace Approximations

A. Derivation of the Spline Approximation

For the sake of simplicity in deriving the algorithm, we assume the order of B-spline is three in this section.

Through (1)–(3), we know that (4) is a quadratic minimization problem. Notice that Φ_2 is different from that of [3], and as discussed in [4] is quadratic. Therefore, a necessary and sufficient condition on the solution is that the gradient of (4) should be zero. Equivalently, we have the following normal equations:

$$\lambda_1\frac{\partial\Phi_1}{\partial c_{mn}} + \lambda_2\frac{\partial\Phi_2}{\partial c_{mn}} + \lambda_3\frac{\partial\Phi_3}{\partial c_{mn}} = 0 \qquad m = 1,2,\ldots,M_x,\ \ n = 1,2,\ldots,M_y. \tag{14}$$

The gradients of these three energy functional is derived in Appendix A, as in (29), (30), and (36). Substituting them into these equations, they are equivalent to

$$\begin{aligned}&2\lambda_1\sum_{i=1}^{N}\left(\sum_{k=1}^{M_x}\sum_{l=1}^{M_y}c_{kl}\beta^3_{kl}(x_i,y_i) - u_i^{\text{int}}\right)\beta^3_{mn}(x_i,y_i)\\ &\quad+2\lambda_2\sum_{i=1}^{N_y}\left(\sum_{k=1}^{M_x}\sum_{l=1}^{M_y}c_{kl}\beta^3_{kl}\left(x_i^{\text{vert}},y_i^{\text{vert}}\right) - \Delta x_i\right)\\ &\quad\times\beta^3_{mn}\left(x_i^{\text{vert}},y_i^{\text{vert}}\right) + 2\lambda_3\sum_{k=1}^{M_x}\sum_{l=1}^{M_y}c_{kl}\sigma_{kl;mn} = 0\end{aligned} \tag{15}$$

or equivalently

$$\begin{aligned}&\lambda_1\sum_{i=1}^{N}\sum_{k=1}^{M_x}\sum_{l=1}^{M_y}\beta^3_k(x_i,y_i)\beta^3_m(x_i,y_i)c_{kl}\\ &\quad+\lambda_2\sum_{i=1}^{N_y}\sum_{k=1}^{M_x}\sum_{l=1}^{M_y}\beta^3_{kl}\left(x_i^{\text{vert}},y_i^{\text{vert}}\right)\beta^3_{mn}\left(x_i^{\text{vert}},y_i^{\text{vert}}\right)c_{kl}\\ &\quad+\lambda_3\sum_{k=1}^{M_x}\sum_{l=1}^{M_y}\sigma_{klmn}c_{kl}\\ &=\lambda_1\sum_{i=1}^{N}u_i^{\text{int}}\beta^3_{mn}(x_i,y_i) + \lambda_2\sum_{i=1}^{N_y}\Delta x_i\beta^3_{mn}\left(x_i^{\text{vert}},y_i^{\text{vert}}\right)\end{aligned} \tag{16}$$

where $m = 1,2,\ldots,M_x$ and $n = 1,2,\ldots,M_y$.

For simplicity, if we denote $k' = kM_x + l$ and $m' = mM_x + n$, k' to order the matrix lexicographically, and $b^2_{k'}(i) = \beta^3_{kl}(x_i,y_i)$ and $\tilde{b}^2_{m'}(i) = \beta^3_{mn}(x_i^{\text{vert}},y_i^{\text{vert}})$, then the above equations can be simplified as

$$\begin{aligned}&\lambda_1\sum_{i=1}^{N}\sum_{k'=1}^{M}b^2_{k'}(i)b^2_{m'}(i)c_{k'}\\ &\quad+\lambda_2\sum_{i=1}^{N_y}\sum_{k'=1}^{M}\tilde{b}^2_{k'}(i)\tilde{b}^2_{m'}(i)c_{k'} + \lambda_3\sum_{k'=1}^{M}\sigma_{k'm'}c_{k'}\\ &=\lambda_1\sum_{i=1}^{N}u_i^{\text{int}}b^2_{m'}(i)\\ &\quad+\lambda_2\sum_{i=1}^{N_y}\delta x_i b^2_{m'}(i),\quad m' = 1,2,\ldots,M\end{aligned} \tag{17}$$

where $M = M_x \times M_y$. Alternatively, we can write these equations in matrix form as

$$\begin{aligned}&(\lambda_1 BB^{\text{T}} + \lambda_2 B^{\text{vert}}(B^{\text{vert}})^{\text{T}} + \lambda_3\Sigma)C\\ &\quad= \lambda_1 BU^{\text{int}} + \lambda_2(B^{\text{vert}})\Delta X\end{aligned} \tag{18}$$

where the matrix $B = (b^2_m(n))_{M\times N}$, $B^{\text{vert}} = (\tilde{b}^2_m(n)_{M\times N_y}$ and $\Sigma_{M\times M}$ are given by

$$B = \begin{pmatrix} b^2_1(1) & b^2_1(2) & \cdots & b^2_1(N)\\ b^2_2(1) & b^2_2(2) & \cdots & b^2_2(N)\\ \vdots & \vdots & \ddots & \vdots\\ b^2_M(1) & b^2_M(2) & \cdots & b^2_M(N)\end{pmatrix} \text{ and}$$

$$B^{\text{vert}} = \begin{pmatrix} \tilde{b}^2_1(1) & \tilde{b}^2_1(2) & \cdots & \tilde{b}^2_1(N_y)\\ \tilde{b}^2_2(1) & \tilde{b}^2_2(2) & \cdots & \tilde{b}^2_2(N_y)\\ \vdots & \vdots & \ddots & \vdots\\ \tilde{b}^2_M(1) & \tilde{b}^2_M(2) & \cdots & \tilde{b}^2_M(N_y)\end{pmatrix}$$

$$\Sigma = \begin{pmatrix} \sigma_{11} & \sigma_{12} & \cdots & \sigma_{1M}\\ \sigma_{21} & \sigma_{22} & \cdots & \sigma_{2M}\\ \vdots & \vdots & \ddots & \vdots\\ \sigma_{M1} & \sigma_{M2} & \cdots & \sigma_{MM}\end{pmatrix}.$$

The column vector U^{int} and ΔX are given by

$$\begin{aligned}(U^{\text{int}})^{\text{T}} =&(u_1^{\text{int}}, u_2^{\text{int}}, \cdots, u_N^{\text{int}}) \text{ and}\\ (\Delta X)^{\text{T}} =&(\delta x_1, \delta x_2, \ldots, \delta x_{N_y}).\end{aligned}$$

The element of BB^{T} is given by

$$c_{k'm'} = \sum_{i=1}^{N} b^2_{k'}(i)b^2_{m'}(i).$$

Due to the local property of B-spline bases, we can conclude that the if the locations of two spline bases are far apart, i.e., if $|k' - m'| > p$ (for cubic spline, $p = 4M_x$), then $c_{k'm'} = 0$. In other words, the matrix BB^{T} is sparse and block-band diagonal since only a few elements are nonzeros. This also holds for $B^{\text{vert}}(B^{\text{vert}})^{\text{T}}$.

Through (35), we know Σ is also diagonal and band limited matrix. Therefore, we can see that the matrix on the left of (18) is sparse, symmetric and positive-definite and we can, therefore, use a fast solver for this linear system of equations. We have

adopted the sparse **Cholesky Factorization** technique [10] to solve this equation. Refer to Appendix B for the description of this algorithm.

In the above derivation we only discuss the solution of the coefficient $\{c_{ij}\}$. Using a similar discussion, we can also show that the solution of $\{d_{ij}\}$ satisfies similar equations as follows:

$$(\lambda_1 BB^{\mathrm{T}} + \lambda_2 B^{\mathrm{hori}}(B^{\mathrm{hori}})^{\mathrm{T}} + \lambda_3 \Sigma)D = \lambda_1 BV^{\mathrm{int}} + \lambda_2 (B^{\mathrm{hori}})\Delta Y \tag{19}$$

where B^{hori} is the matrix of splines defined on the horizontal tag lines and

$$(V^{\mathrm{int}})^{\mathrm{T}} = (v_1^{\mathrm{int}}, v_2^{\mathrm{int}}, \ldots, v_N^{\mathrm{int}}) \text{ and}$$
$$(\Delta Y)^{\mathrm{T}} = (\delta y_1, \delta y_2, \ldots, \delta y_{N_y}).$$

Once we get the solution of $\{c\}$ and $\{d\}$, we could estimate the deformation of LV at any dense points using formula (5).

B. Computation of Smoothness Terms

For illustration, we only give the details on how to compute the smoothness terms (32) by taking advantage of spline properties.

Through properties (11)–(13) it is easy to show that

$$\begin{aligned}\int \beta_k^3(y)\beta_l^3(y)dy &= \int \beta^3(y+n-l)\beta^3(y)dy \\ &= \int \beta^3(y+n-l)\beta^3(-y)dy \\ &= \int \beta^3(n-l-t)\beta^3(t+4)dt \\ &= (\beta^3 * \beta^3)(n-l+4) = b^7(n-l+4)\end{aligned}$$

and

$$\begin{aligned}&\int (\beta_k^3)''(x)\,(\beta_m^3)''(x)dx \\ &= \int \left(\beta_k^1(x) - 2\beta_k^1(x-1) + \beta_k^1(x-2)\right) \\ &\quad \times \left(\beta_m^1(x) - 2\beta_m^1(x-1) + \beta_m^1(x-2)\right)dx \\ &= \int \beta_k^1(x)\beta_m^1(x)dx - 2\int \beta_k^1(x)\beta_{m+1}^1(x)dx \\ &\quad + \int \beta_k^1(x)\beta_{m+2}^1(x)dx - 2\int \beta_{k+1}^1(x)\beta_m^1(x)dx \\ &\quad + 4\int \beta_{k+1}^1(x)\beta_{m+1}^1(x)dx - 2\int \beta_{k+1}^1(x)\beta_{m+2}^1(x)dx \\ &\quad + \int \beta_{k+2}^1(x)\beta_m^1(x)dx - 2\int \beta_{k+2}^1(x)\beta_{m+1}^1(x)dx \\ &\quad + \int \beta_{k+2}^1(x)\beta_{m+2}^1(x)dx \\ &= b^3(m-k+2) - 2b^3(m+3-k) \\ &\quad + b^3(m+4-k) - 2b^3(m-k+1) \\ &\quad + 4b^3(m+2-k) - 2b^3(m+3-k) + b^3(m-k) \\ &\quad - 2b^3(m+1-k) + b^3(m+2-k) \\ &= 6b^3(m-k+2) - 4b^3(m-k+3) \\ &\quad + b^3(m-k+4) - 4b^3(m-k+1) + b^3(m-k).\end{aligned}$$

TABLE I
THE 13 k-PARAMETERS OF THE KINEMATIC MODEL

k_1	Radially dependent compression
k_2	Left ventricular torsion
k_3	Ellipticalization in long-axis (LA) planes
k_4	Ellipticalization in short-axis (SA) planes
k_5	Shear in x direction
k_6	Shear in y direction
k_7	Shear in z direction
k_8	Rotation about x-axis
k_9	Rotation about y-axis
k_{10}	Rotation about z-axis
k_{11}	Translation in x direction
k_{12}	Translation in y direction
k_{13}	Translation in z direction

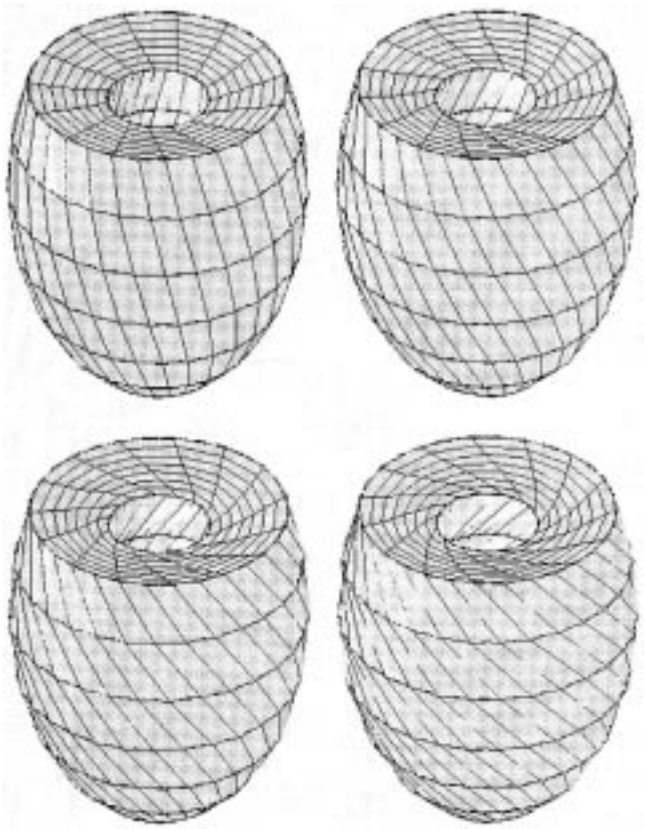

Fig. 2. Deformed models of the LV resulting from change of k_2 from 0.2 to 0.8 in increments of 0.2.

Therefore, we have

$$\begin{aligned}\sigma_{kl;mn}^{(1)} = b^7(n-l+4)(&6b^3(m-k+2) - 4b^3(m-k+3) \\ &+ b^3(m-k+4) - 4b^3(m-k+1) + b^3(m-k)).\end{aligned} \tag{20}$$

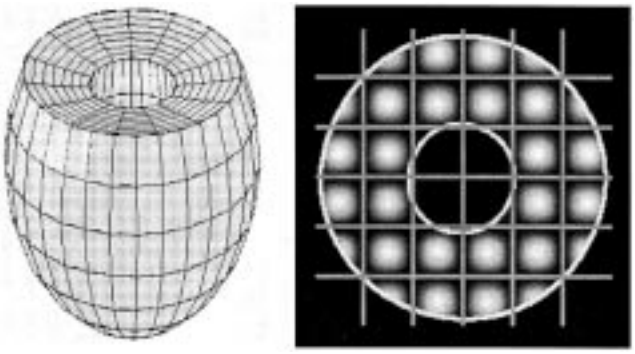

Fig. 3. The undeformed prolate spheroidal model of the LV in the reference state. A tagged image corresponding to a selected imaging plane is shown on the right. The width of the "donut" is about 1.5 cm, and the discretization step is 0.05 cm.

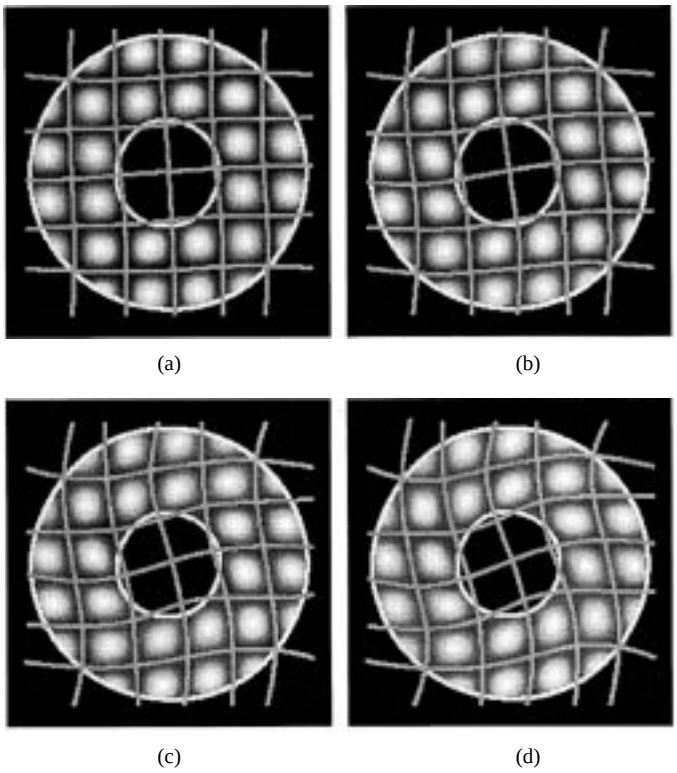

(a) (b)

(c) (d)

Fig. 4. Results of coupled B-snake tracker on a simulated image sequence ($\beta_1 = 75$, $\beta_2 = 1$). From top-left ($k_2 = 0.2$) to bottom-right ($k_2 = 0.8$) in increments of 0.2. Temporal resolution is 20 ms.

Similarly, we can derive that

$$\begin{aligned}\sigma^{(2)}_{kl;mn} =&(-b^5(m-k+2)+2b^5(m-k+3)\\ &-b^5(m-k+4))(-b^5(n-l+2)\\ &+2b^5(n-l+3)-b^5(n-l+4))\end{aligned} \tag{21}$$

and

$$\begin{aligned}\sigma^{(3)}_{kl;mn} =&b^7(m-k+4)(6b^3(n-l+2)-4b^3(n-l+3)\\ &+b^3(n-l+4)-4b^3(n-l+1)+b^3(n-l)).\end{aligned} \tag{22}$$

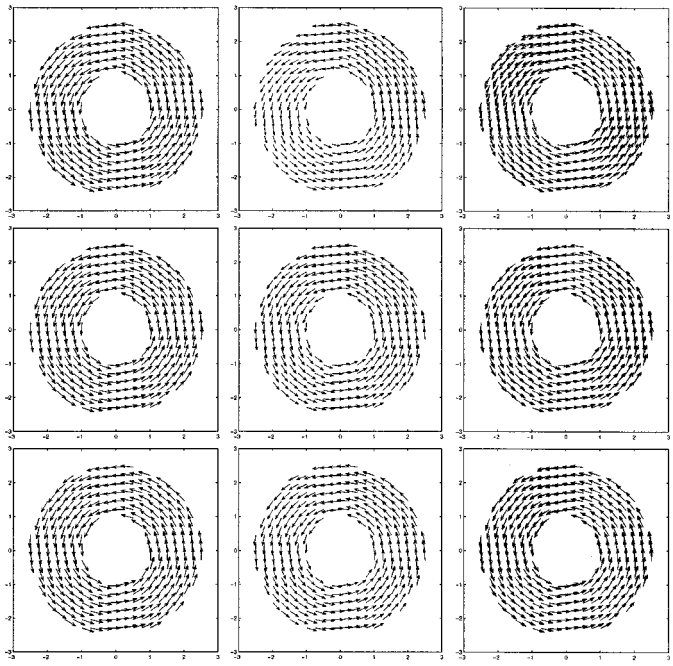

Fig. 5. Comparison of computed (left column) and true (middle column) displacement vector fields corresponding to torsion [from $k_2 = 0.03$ (top) to $k_2 = 0.15$ (bottom)]. Third column is an overlap display.

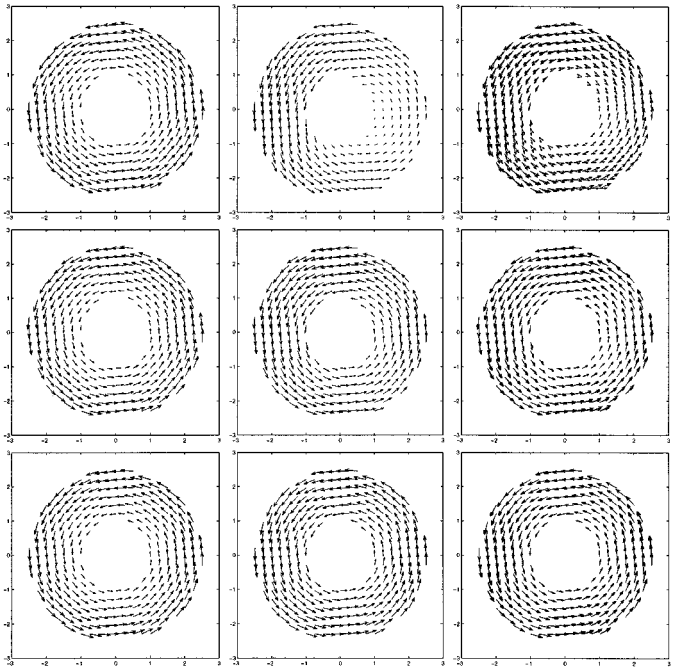

Fig. 6. Comparison of computed (left column) and true (middle column) displacement vector fields corresponding to rotation [from $k_{10} = -0.04$ (top) to $k_{10} = -0.2$ (bottom)]. Third column is an overlap display.

So we only need to evaluate the values of B-splines of order three, five, and seven at integers in order to compute these quantities. The algorithm for computation of the values of these discrete B-splines at integres is described in Appendix C.

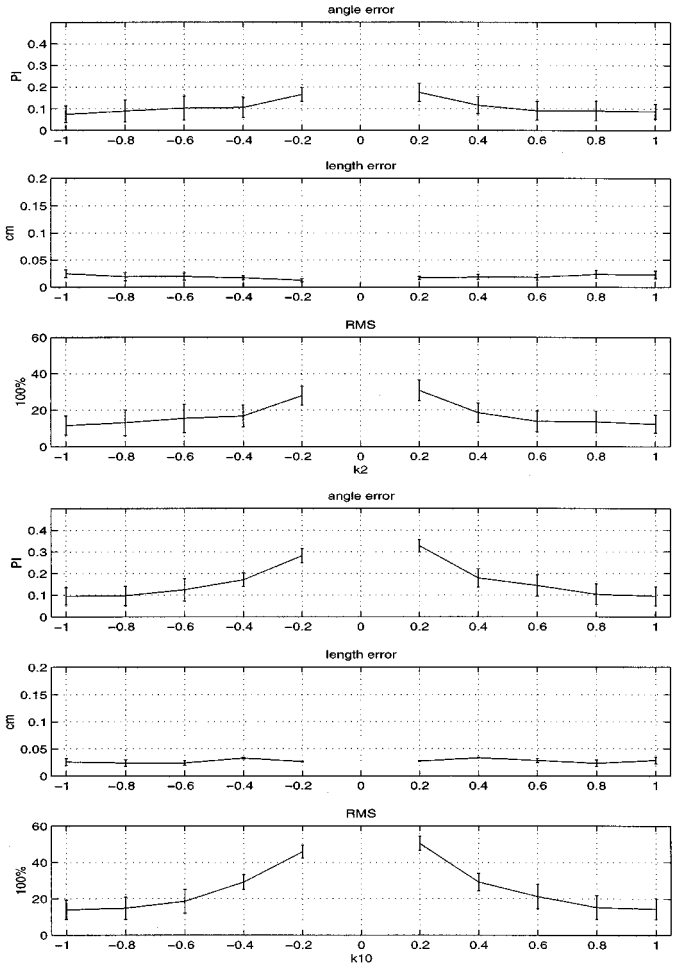

Fig. 7. The statistical error plots for length, angle and relative rms errors for k_2, and k_{10}. See text for details.

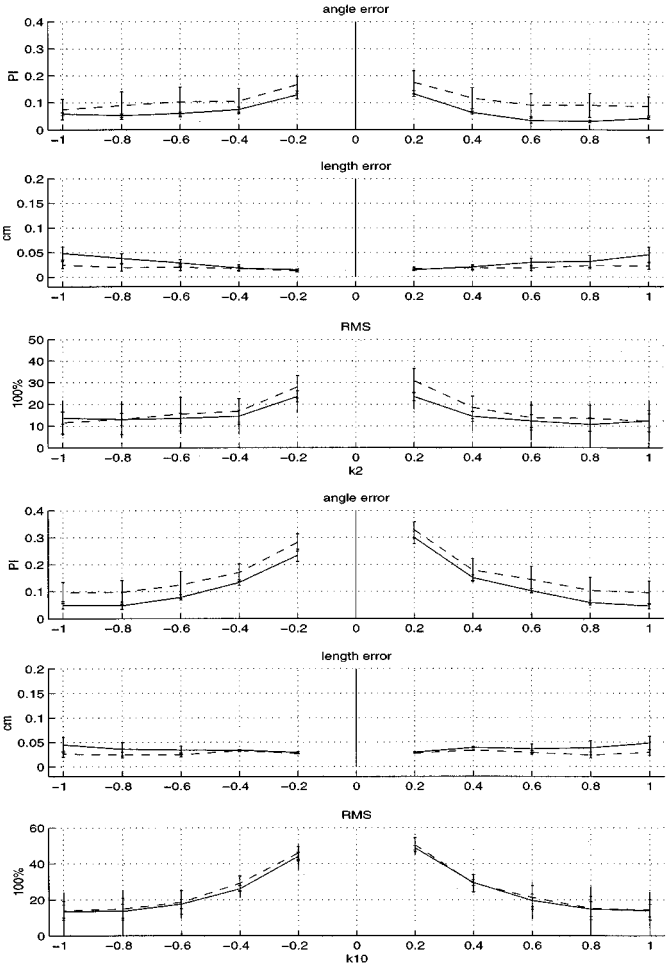

Fig. 8. A comparison between this method (solid line) and the one in [3] (dotted line) for length, angle and relative rms errors for k_2, and k_{10}. See text for details.

V. Validation

A. Cardiac Simulator

An environment based on a 13-parameter kinematic model of Arts *et al.* [5] has been implemented for simulating a time sequence of tagged MR images at arbitrary orientation, as was described in [21]. Through the discretization of the space between two concentric shells and by varying the canonical parameters of the model, both a sequence of tagged MR images as well as a "ground truth" vector field of actual material point deformations are available.

A pair of prolate spheroid represents the endocardial and epicardial LV surfaces, and provides a geometric model of the LV myocardium. The motion model involves application of a cascade of in-compressible linear transformations describing rigid as well as nonrigid motions. The parameters of the motion model, referred to as k-parameters, and the transformations to which they correspond are stated in Table I. Fig. 2 displays a sequence of 3-D deformed LV models resulting from change of k_2 parameter, which corresponds to torsion of the prolate spheroid.

In order to simulate MR images, an imaging plane intersecting the geometric model is selected, and tagged spin-echo imaging equations are applied for simulating the *in vivo* imaging process. Fig. 3 displays an undeformed 3-D model (with all the k-parameters identical to zero) and a simulated tagged image corresponding roughly to the middle of the LV. Fig. 4 shows the deformed tag image slices, which intersect the deformed LV models in Fig. 2. Also, this figure shows the detected tag lines using the coupled B-spline tracker [3].

TABLE II
A Comparison of Computational Speed (in Minutes) on a Sun Ultra 30/300-MHz Workstation

Frame No.	1	2	3	4	5
New method	1.09	1.09	1.10	1.10	1.10
Previous method [3]	19.44	19.30	24.46	23.25	26.19

For k_2

Frame No.	1	2	3	4	5
New method	1.11	1.10	1.10	1.09	1.10
Previous method [3]	36.25	17.58	24.33	25.36	23.46

For k_{10}

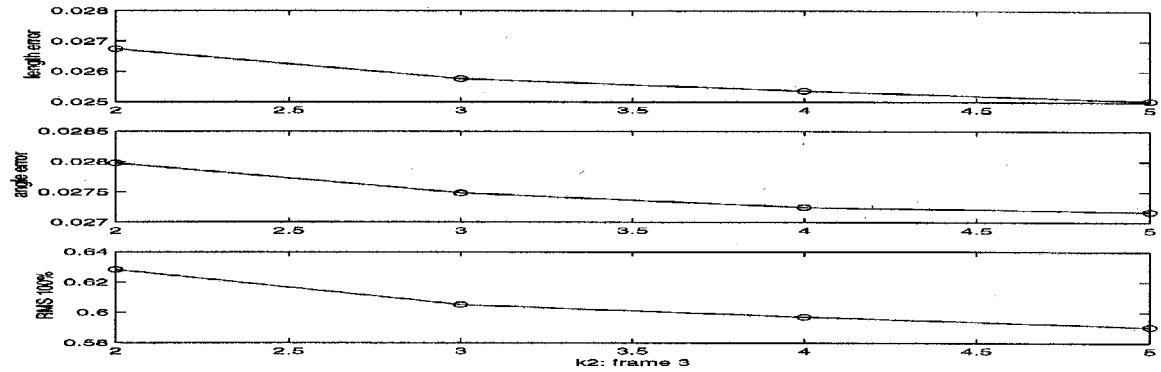

$$k_2 = 0.15$$

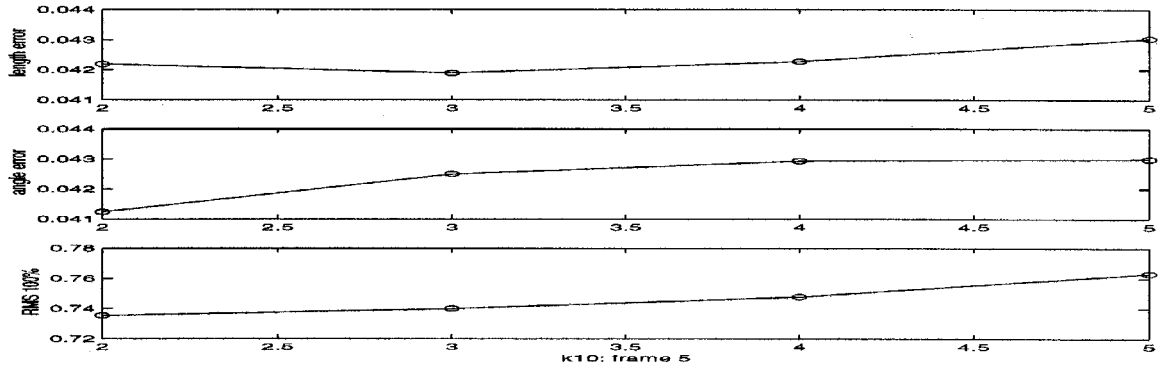

$$k_{10} = -0.2$$

Fig. 9. The influence of the order of B-spline bases on the reconstructions of vector field. The errors are plotted as a function of the order of B-splines. Here, we take $\lambda_1 = 1$, $\lambda_2 = 2$, and $\lambda_3 = 1$.

For the purposes of validating 2-D displacement field reconstructions, we have used the parameters k_2, k_4, k_5, and k_{10} for generating 2-D deformations of the geometric model, based on which images and 2-D displacement vector fields of *actual* material points are produced. The error norms used in comparing the ground truth vector field (V_g) with the vector field measured by our algorithm (V_m) are

$$\varepsilon_L = \frac{1}{N} \sum ||V_m| - |V_g|| \tag{23}$$

and

$$\varepsilon_\theta = \frac{1}{\sum |V_g|} \sum |V_g| \cdot \arccos \frac{V_g \cdot V_m}{|V_g||V_m|} \tag{24}$$

where ε_L measures the average difference in length between V_g and V_m, and ε_θ measures the deviation in angle between V_g and V_m. As can be seen from (24), we weight individual angle deviations by the magnitude of the material point displacement vector; normalized by the sum of magnitude of all ground truth vectors. The reason for this is to emphasize angle deviation of points which have large displacements, and similarly to de-emphasize the angle deviation of points which have a smaller displacement.

We also employ the relative root mean squared (rms) figure of merit to measure the accuracy of the computed motion fields

$$\varepsilon_r = \frac{\sqrt{(1/N) \sum |V_m - V_g|^2}}{(1/N) \sum |V_g|} \times 100\% \tag{25}$$

where N is the number of vectors in the field.

B. Results

Fig. 2 shows an example of the deformed models of the LV which result from change of the k_2 parameters, torsion, from 0.2 to 0.8 in increments of 0.2. Fig. 4 shows the corresponding tag tracking results of these simulated image sequences. In Fig. 5 we compare the computed and ground truth displacement vector fields that correspond to this image plane. One can visually appreciate the high accuracy of the reconstructions. Fig. 6 shows another example of the vector field reconstruction for the case of rigid rotation.

In order to measure the accuracy quantitatively, we plot the length errors, angle errors as well as the relative rms in Fig. 7 by comparing V_m and V_g as a function of a range of values of k_2 and k_{10}, keeping the rest of the k parameters constant. Additionally, as part of the validations and in order to test the sensitivity of the algorithms to different values of algorithm coefficients λ_1, λ_2, and λ_3, we varied each of these coefficients

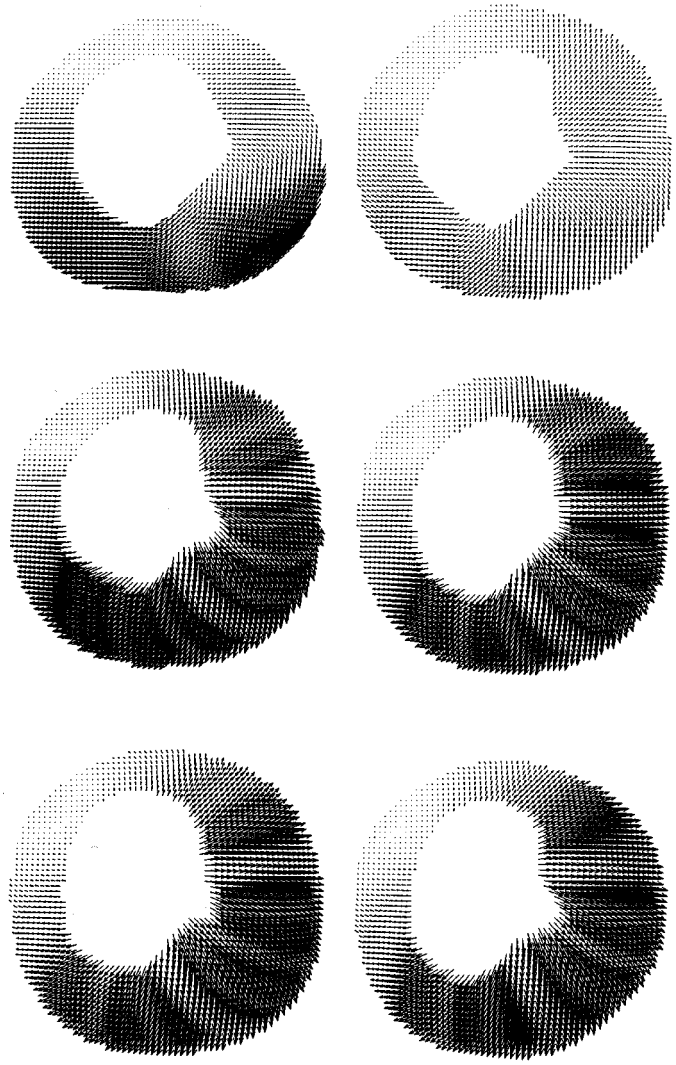

Fig. 10. Six displacement vector fields from *in vivo* tagged slices of a patient with antero-septal MI at 29, 58, 87, 116, 145, and 174 ms after the ECG R wave. (The slices in this and following figures are ordered from left to right and top to bottom). Segmental motion of all myocardial points can be easily quantitated and visualized from the location, direction, and length of the displayed vectors.

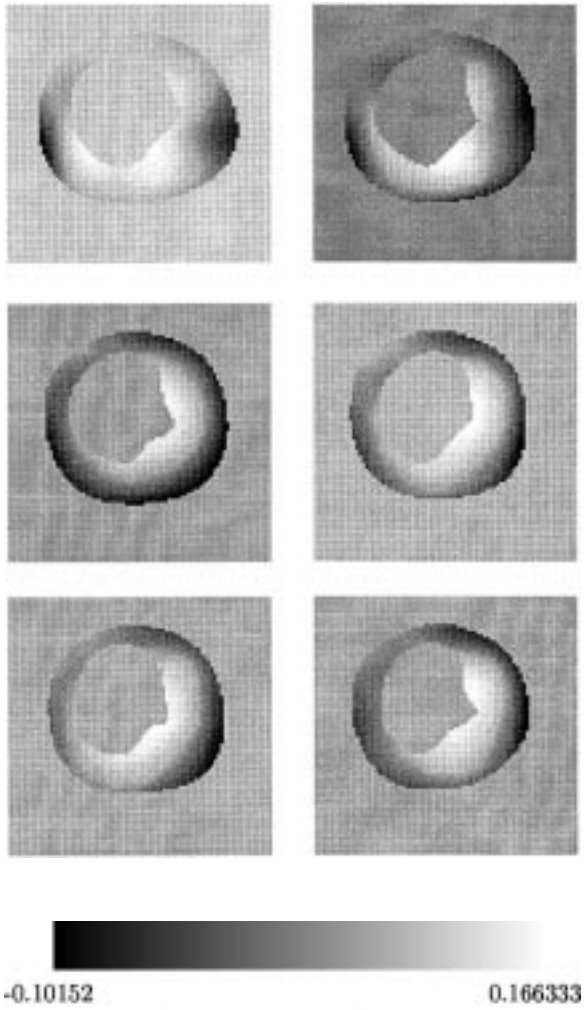

Fig. 11. The figure shows the computed radial strains corresponding to the same time points as in Fig. 10.

individually in the range $\{0, 1, \ldots, 10\}$, and kept the other two coefficients at the constant value of one (excluding $\lambda_1 = 0$). The experiment is performed on 32 parameters, and the mean and variance of each error measure is computed to test the influence of these parameters. The error bars in these plots show the 3σ range on either side of the error mean for particular values of each k parameter. As can be seen from the figures, to a large degree the displacement reconstruction algorithm is insensitive to the exact values of λ_is. An additional remarkable point regarding the error plots is the fact that for smaller motions, the value of ε_θ is larger than that for bigger motions. The reason for this nonintuitive result can only be attributed to the larger percent inaccuracies in reconstruction of smaller displacements by the warping algorithm. Also, it should be noted that error plots in Fig. 7 subsume the errors incurred in localization of tags and myocardial contours (for these validations, tag and contour localization is performed through semi-automated determination of control points of B-spline grids [3]). Although the magnitude of errors are bound to be smaller if accurate location of contour and tag lines in the simulated images were to be used, our complete system for tracking and reconstruction of tag lines would not be tested, and furthermore since the exact location of tags and contours are not known in real images, phantom validation results would not be a good model of realistic situations.

In order to test the influence of the order of B-spline bases on the reconstruction, we plot in Fig. 9 the errors as a function of order of B-splines in the case of k_2 and k_{10}. As can be seen, the orders of the B-splines do not have much influence on the reconstruction accuracy.

To compare the performance of the proposed method with that of [3], we list the computational time in Table II. As seen, significant savings in time is achieved. In the meantime, we obtain similar accuracy as before, as shown in Fig. 8.

C. In Vivo Validations

A segmented k-space SPAMM pulse sequence with breathhold was used to collect images from a porcine model of

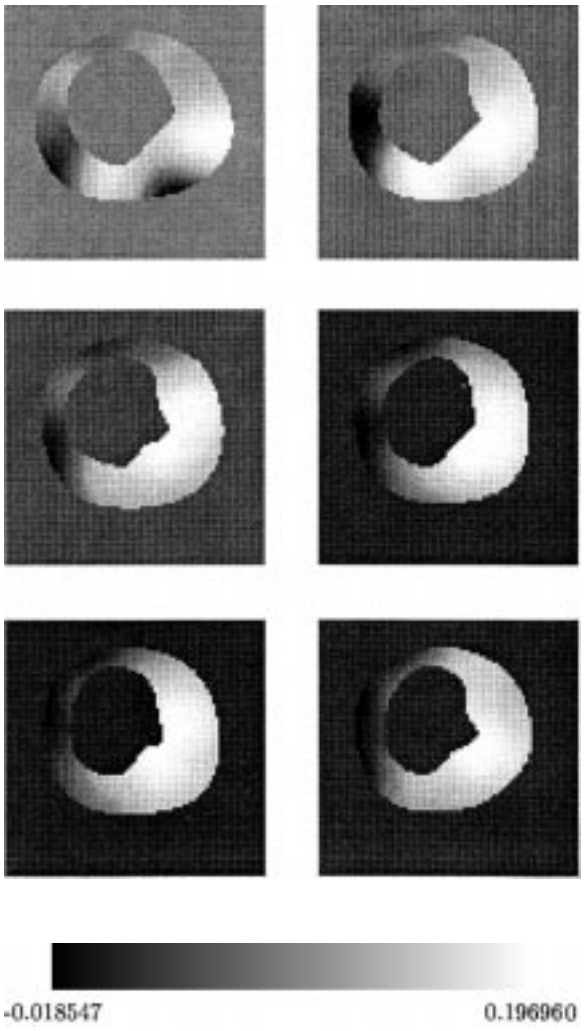

Fig. 12. The figure shows the circumferential strains corresponding to the same time points as in Fig. 10.

myocardial infraction. For MR imaging, multiple images in short-axis (SA) views of the heart were collected to cover the entire volume without gaps. Immediately after the electrocardiogram (ECG) trigger, radio-frequency (RF) tagging pulses were applied in two orthogonal directions. The repetition time (TR) of the imaging sequence was approximately 7.1 ms, the echo time (TE) was 2.9 ms, and the RF pulse flip angle was 15°. Echo sharing was used in collecting each time-varying image sequence for given slice position. Five data lines were collected for any time frame during each heart cycle, but two data lines were overlapped between two consecutive cardiac frames, resulting in an effective temporal resolution of approximately 22 ms. Other imaging parameters were: field of view= 300 mm, data acquisition matrix size= 250 × 256 (phase encoding by readout), in-plane resolution in-plane resolution= 1.2 × 1.17 mm^2, slice thickness= 7 mm, and tag spacing = 7 mm. The tag and contour lines are traced in a semi-automatic envoriment by determining location of B-spline control points [3].

Figs. 10–15 show examples of the computation of motion fields and corresponding strains in a patient with an old MI, and a pig immediately after induction of a postero-lateral MI. The

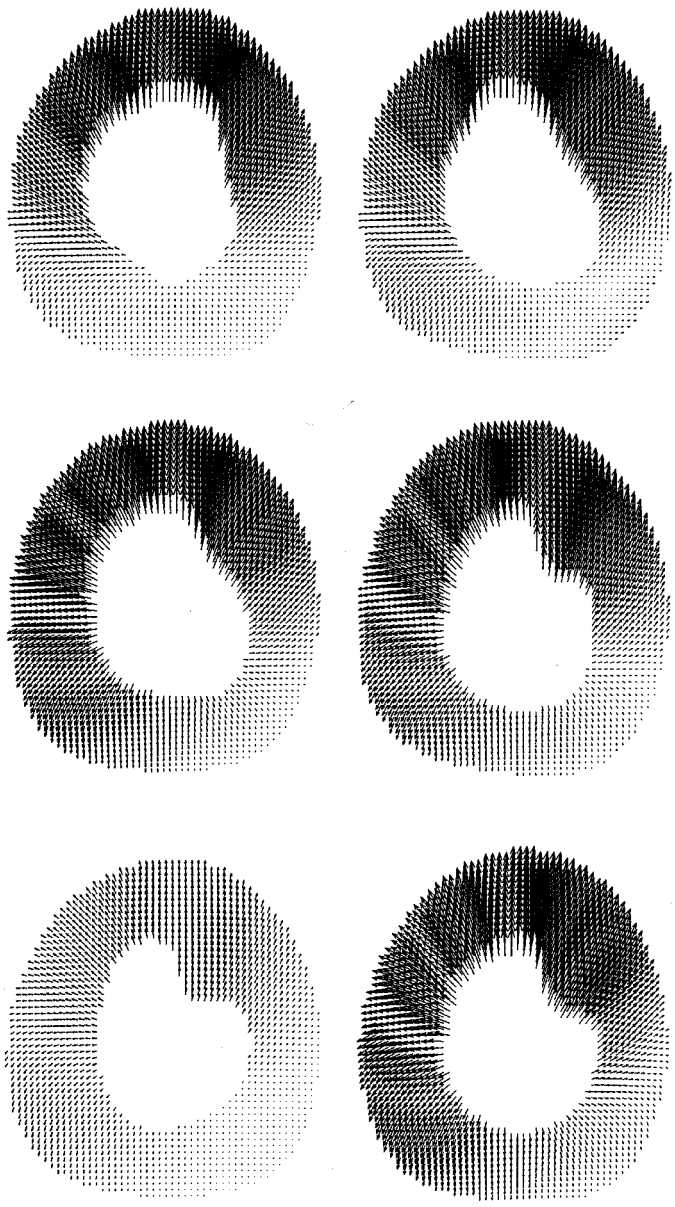

Fig. 13. Six displacement vector fields for *in vivo* tagged slices for a pig immediately after induction of a postero-lateral myocardial infarction. Segmental motion of all myocardial points can be easily quantitated and visualized from the location, direction, and length of the displayed vectors. Specifically, notice the consistently small magnitude of the vector field in the infarct area (between 3 and 7 o'clock positions).

segmental motion of all myocardial points can be easily quantitated and visualized from the location, direction, and length of the displayed vectors.

D. Myocardial Strains

Starting at any time point during the cardiac cycle, as in [4], the heart's motion is viewed in the Eulerian reference frame; i.e., a mapping which warps the *deformed* tag configuration into the *undeformed* configuration $\mathbf{X} = \mathbf{\Gamma}(\mathbf{x})$. Equivalently, with $\mathbf{X} = \mathbf{V}(\mathbf{x}) + \mathbf{x}$, the deformation gradient tensor can be written as $\mathbf{F} = \nabla\mathbf{\Gamma}(\mathbf{x}) = \nabla\mathbf{V}(\mathbf{x}) + \nabla\mathbf{x}$ where $\mathbf{V}$ is the computed displacement vector field. Note that the out-of-plane motion of

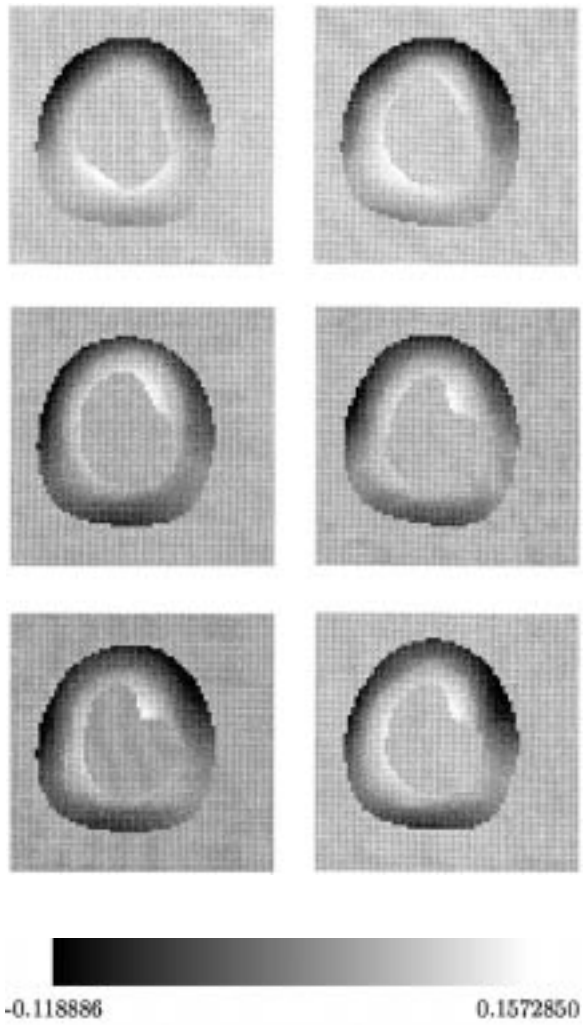

Fig. 14. The figure shows the computed radial strains corresponding to the same time points as in Fig. 13.

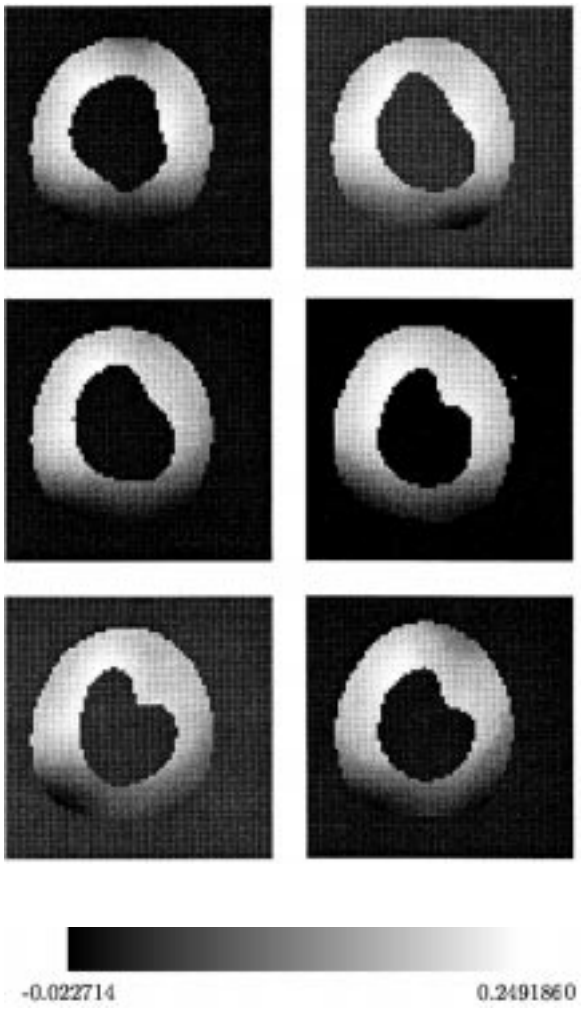

Fig. 15. The figure shows the circumferential strains corresponding to the same time points as in Fig. 13. The area between 3 and 7 o'clock positions exhibit small strain values indicative of akinesis.

the heart near the apex is small and the method could be directly applicable to the case of looking at motion fields in short axis slices near the apex without any loss of accuracy. Therefore, assuming little or no through-plane motion

$$\mathbf{F} = \begin{pmatrix} u_x + 1 & u_y \\ v_x & v_y + 1 \end{pmatrix} \tag{26}$$

And, the strain tensor, as shown in (27) at the bottom of the page. Once a displacement vector field is available, the strain of deformation can be computed at all myocardial points within a SA slice. Furthermore, the quantity $\mathbf{M}^{\mathrm{T}}\mathbf{E}\mathbf{M}$ will give the value of strain for the direction $\mathbf{M}$.

Figs. 11, 12, 14, and 15 are the radial and circumferential strains corresponding to the same time points as those in Figs. 10 and 13.

VI. Conclusion

In conclusion, we have described a very efficient computational algorithm for analysis of SPAMM tagged data. The new methods take advantage of B-spline properties, such as the the local support and smoothness. The representations of displacement vector fields using B-spline bases result in a compact form and the coefficients can be determined uniquely and efficiently using fast algorithms. Because of the local and compact support of B-spline bases, the local deformation of LV is well

$$\begin{aligned} \mathbf{E} &= \frac{1}{2}\left(\mathbf{F}^{\mathrm{T}}\mathbf{F} - \mathbf{I}\right) \\ &= \begin{pmatrix} u_x + \frac{1}{2}\left(u_x^2 + v_x^2\right) & \frac{1}{2}(u_y + v_x + u_x u_y + v_x v_y) \\ \frac{1}{2}(u_y + v_x + u_x u_y + v_x v_y) & v_y + \frac{1}{2}\left(u_y^2 + v_y^2\right) \end{pmatrix}. \end{aligned} \tag{27}$$

represented using such bases. Moreover, one can increase the smoothness of vector fields easily by simply changing the order of B-spline bases. The derivation of the algorithms for any orders of B-splines has been presented in the paper. Most importantly, the proposed algorithm can be implemented in fast time, which is important for clinical use.

In addition to the developed machinery in this paper, evaluation of the methods have been tested using both simulated and *in vivo* data sets. The algorithm was tested for accuracy in length and angles well as the relative rms of the reconstructed displacement vectors from the known ground-truth, and the results indicate that the reconstructions of myocardial deformations are sufficiently accurate for measurement of in-plane tissue deformations in fast time and at any time frame in a sequence of tagged images. The extension of methods to 3-D is the topic of current research.

Appendix A
Derivation of Gradient of Energy Functions

If the vector field is represented as (5), then (1) becomes

$$\Phi_1(u,v)=\sum_{i=1}^{N}\left\{\left(\sum_{k=1}^{M_x}\sum_{l=1}^{M_y}c_{kl}\beta_{kl}^3(x_i,y_i)-u_i^{\text{int}}\right)^2+\left(\sum_{k=1}^{M_x}\sum_{l=1}^{M_y}d_{kl}\beta_{kl}^3(x_i,y_i)-v_i^{\text{int}}\right)^2\right\} \tag{28}$$

where (x_i,y_i), $i=1,2,\ldots,N$ are the coordinates of deformed tag intersections.

If we take the derivative of Φ_1 with respect to coefficient $c_{k^*l^*}$, we obtain

$$\begin{aligned}\frac{\partial\Phi_1}{\partial c_{k^*l^*}}=&2\sum_{i=1}^{N}\left(\sum_{k=1}^{M_x}\sum_{l=1}^{M_y}c_{kl}\beta_{kl}^3(x_i,y_i)-u_i^{\text{int}}\right)\\&\times\beta_{k^*l^*}^3(x_i,y_i),\\ k^*=&1,2,\ldots,M_x,\ \ l^*=1,2,\ldots,M_y.\end{aligned} \tag{29}$$

Similarly, for Φ_2 we have

$$\begin{aligned}&\Phi_2(u,v)\\&=\sum_{i=1}^{N_y}\left(x_i^{\text{vert}}+\sum_{k=1}^{M_x}\sum_{l=1}^{M_y}c_{kl}\beta_{kl}^3\left(x_i^{\text{vert}},y_i^{\text{vert}}\right)-\bar{x}_i\right)^2\\&\quad+\sum_{i=1}^{N_x}\left(y_i^{\text{hori}}+\sum_{k=1}^{M_x}\sum_{l=1}^{M_y}d_{kl}\beta_{kl}^3\left(x_i^{\text{hori}},y_i^{\text{hori}}\right)-\bar{y}_i\right)^2\\&=\sum_{i=1}^{N_y}\left(\sum_{k=1}^{M_x}\sum_{l=1}^{M_y}c_{kl}\beta_{kl}^3\left(x_i^{\text{vert}},y_i^{\text{vert}}\right)-\Delta x_i\right)^2\\&\quad+\sum_{i=1}^{N_x}\left(\sum_{k=1}^{M_x}\sum_{l=1}^{M_y}d_{kl}\beta_{kl}^3\left(x_i^{\text{hori}},y_i^{\text{hori}}\right)-\Delta y_i\right)^2\end{aligned}$$

where $(x_i^{\text{hori}},y_i^{\text{hori}})$, $i=1,2,\ldots,N_x$ and $(x_i^{\text{vert}},y_i^{\text{vert}})$, $i=1,2,\ldots,N_y$ are the coordinates of deformed tag lines along the horizontal and vertical directions, respectively. $(\bar{x}_i,\bar{y}_i)$ are the coordinates of the undeformed tag lines. $\Delta x_i=x_i^{\text{vert}}-\bar{x}_i$ and $\Delta y_j=y_j^{\text{hori}}-\bar{y}_j$.

The derivative of Φ_2 with respect to $c_{k^*l^*}$ is given by

$$\begin{aligned}\frac{\partial\Phi_2}{\partial c_{k^*l^*}}=&2\sum_{i=1}^{N_y}\left(\sum_{k=1}^{M_x}\sum_{l=1}^{M_y}c_{kl}\beta_{kl}^3\left(x_i^{\text{vert}},y_i^{\text{vert}}\right)-\Delta x_i\right)\\&\times\beta_{k^*l^*}^3\left(x_i^{\text{vert}},y_i^{\text{vert}}\right),\\ k^*=&1,2,\ldots,M_x,\ \ l^*=1,2,\ldots,M_y.\end{aligned} \tag{30}$$

Let us consider Φ_3. For the convenience of derivation, Φ_3 can be split into two parts: $\Phi_3=\Phi_3^{(1)}+\Phi_3^{(2)}$, where $\Phi_3^{(1)}=\int\int(u_{xx}^2+2u_{xy}^2+u_{yy}^2)dxdy$ and $\Phi_3^{(2)}=\int\int(v_{xx}^2+2v_{xy}^2+v_{yy}^2)dxdy$. We only need to consider the computation of the first part $\Phi_3^{(1)}$ since $\Phi_3^{(2)}$ can be treated similarly.

Substituting (5) into, (3) we obtain

$$\begin{aligned}\Phi_3^{(1)}=&\int\int\left(u_{xx}^2+2u_{xy}^2+u_{yy}^2\right)dxdy\\=&\int\int\left(\sum_{j=1}^{M_x}\sum_{j=1}^{M_y}c_{ij}\left(\beta_i^3(x)\right)''\beta_j^3(y)\right)^2dxdy\\&+2\int\int\left(\sum_{j=1}^{M_x}\sum_{j=1}^{M_y}c_{ij}\left(\beta_i^3(x)\right)'\left(\beta_j^3(y)\right)'\right)^2dxdy\\&+\int\int\left(\sum_{j=1}^{M_x}\sum_{j=1}^{M_y}c_{ij}\beta_i^3(x)\left(\beta_j^3(y)\right)''\right)^2dxdy\\=&\sum_{k=1}^{M_x}\sum_{l=1}^{M_y}\sum_{m=1}^{M_x}\sum_{n=1}^{M_y}c_{kl}c_{mn}\\&\times\left(\sigma_{kl;mn}^{(1)}+2\sigma_{kl;mn}^{(2)}+\sigma_{kl;mn}^{(3)}\right)\\=&\sum_{k=1}^{M_x}\sum_{l=1}^{M_y}\sum_{m=1}^{M_x}\sum_{n=1}^{M_y}c_{kl}c_{mn}\sigma_{kl;mn}\end{aligned} \tag{31}$$

where we denote $\sigma_{kl;mn}=\sigma_{kl;mn}^{(1)}+2\sigma_{kl;mn}^{(2)}+\sigma_{kl;mn}^{(3)}$ and

$$\begin{aligned}\sigma_{kl;mn}^{(1)}=&\int\int(\beta^3)_k''(x)\beta_l^3(y)(\beta^3)_m''(x)\beta_n^3(y)dxdy\\=&\int(\beta^3)_k''(x)(\beta^3)_m''(x)dx\int\beta_l^3(y)\beta_n^3(y)dy,\end{aligned} \tag{32}$$

$$\begin{aligned}\sigma_{kl;mn}^{(2)}=&\int\int(\beta^3)_k'(x)(\beta^3)_l'(y)(\beta^3)_m'(x)(\beta^3)_n'(y)dxdy\\=&\int(\beta^3)_k'(x)(\beta^3)_m'(x)dx\int(\beta^3)_l'(y)(\beta^3)_n'(y)dy,\end{aligned} \tag{33}$$

$$\begin{aligned}\sigma_{kl;mn}^{(3)}=&\int\int\beta_k^3(x)(\beta^3)_l''(y)\beta_m^3(x)(\beta^3)_n''(y)dxdy\\=&\int\beta_k^3(x)\beta_m^3(x)dx\int(\beta^3)_l''(y)(\beta^3)_n''(y)dy.\end{aligned} \tag{34}$$

From the local support $[0,4]$ of cubic B-splines, it is also not hard to show that

$$\begin{aligned}&\sigma_{kl;mn}^{(1)}=\sigma_{kl;mn}^{(2)}=\sigma_{kl;mn}^{(3)}=0,\\&\text{if } |k-m|>4 \text{ or } |n-l|>4.\end{aligned} \tag{35}$$

The derivative of Φ_3 with respect to coefficient $c_{k^*l^*}$ is

$$\frac{\partial \Phi_3}{\partial c_{k^*l^*}} = 2\sum_{k=1}^{M_x}\sum_{l=1}^{M_y} c_{kl}\sigma_{k,l;k^*l^*},$$
$$k^* = 1,2,\ldots,M_x, l^* = 1,2,\ldots,M_y. \tag{36}$$

Appendix B
Band Cholesky Decomposition and Complexity Analysis

In this Appendix, we give an overview of the Choleskey Decomposition method or square root method. For details, refer to [10].

A symmetric and positive definite matrix can be efficiently decomposed into a lower and upper triangular matrix. For a matrix of any type, this is achieved by the LU decomposition which factorizes $A = LU$. In addition, if A is symmetric and positive definite, it can be decomposed more efficiently into $A = U^tU$, where U (which can be seen as the "square root" of A) is a lower triangular matrix with positive diagonal elements. To solve $Ax = b$, one solves first $Uy = b$ for y, and then $U^{\mathrm{T}}x = y$ for x. i.e.,

$$\begin{pmatrix} a_{11} & a_{12} & \cdots & a_{1M} \\ a_{21} & a_{22} & \cdots & a_{2M} \\ \vdots & \vdots & \ddots & \vdots \\ a_{M1} & a_{M2} & \cdots & a_{MM} \end{pmatrix} = \begin{pmatrix} u_{11} & 0 & \cdots & 0 \\ u_{21} & u_{22} & \cdots & 0 \\ \vdots & \vdots & \ddots & \vdots \\ u_{M1} & u_{M2} & \cdots & u_{MM} \end{pmatrix} \cdot \begin{pmatrix} u_{11} & u_{12} & \cdots & u_{M1} \\ 0 & u_{22} & \cdots & u_{M2} \\ \vdots & \vdots & \ddots & \vdots \\ 0 & 0 & \cdots & u_{MM} \end{pmatrix}. \tag{37}$$

We then can obtain the element of U as follows:

$$u_{11} = \sqrt{a_{11}} \tag{38}$$
$$u_{ii} = \left(a_{ii} - \sum_{k=0}^{i-1} u_{ki}^2\right)^{(1/2)}, \quad i = 2,\ldots,M-1,$$
$$u_{ij} = \frac{a_{ij} - \sum_{k=1}^{M} u_{ik}u_{kj}}{u_{ii}}, \quad j > i \tag{39}$$

Because A is symmetric and positive definite, the expression under the square root is always positive, and all u_{ij} are real (see [10]). Then the solution of $AX = B$ is given by

$$y_i = \frac{b_i - \sum_{k=0}^{i-1} u_{ki}y_k}{u_{ii}} \tag{40}$$
$$x_i = \frac{y_i - \sum_{k=i+1}^{M-1} u_{ki}x_k}{u_{ii}}. \tag{41}$$

Moreover, since the matrix is also banded with bandwidth p, we can further reduce the computation and storage. See [10, Algorithm 4.3.5.] for more details. If $M \gg p$ then this algorithm can be implemented in linear time which requires about $M(p^2+3p)$ flops and M square roots. In addition, we could simply store the nonzero lower triangular part, then a $(p+1)$-by-M array would suffice.

Appendix C
Computation of Discrete B-Spline Values at Integers

We derive the exact formula for the computation of $b^n(k) = \beta^n(k)$ of different orders. We consider the z transform of these sequences. By the definition (7), we have

$$\begin{aligned} B^n(z) &= \sum_{k=1}^{n} b^n(k)z^{-k} \\ &= \sum_{j=0}^{n+1} \frac{(-1)^j}{n!}\binom{n+1}{j}\sum_{k\in Z}(k-j)^n\mu(k-j)z^{-k} \\ &= \sum_{j=0}^{n+1} \frac{(-1)^j}{n!}\binom{n+1}{j}\sum_{k\geq j}(k-j)^n z^{-k} \\ &= \sum_{j=0}^{n+1} \frac{(-1)^j}{n!}\binom{n+1}{j}\sum_{l=0}^{n+1} l^n z^{-(l+j)} \\ &= \sum_{j=0}^{n+1} \frac{(-1)^j}{n!}\binom{n+1}{j} z^{-j}\sum_{l=0}^{\infty} l^n z^{-l} \\ &= (1-z^{-l})^{n+1}\sum_{l=0}^{\infty} l^n z^{-l}. \end{aligned}$$

Since

$$\sum_{l=0}^{\infty} l^n z^{-l} = \frac{\left(\sum_{l=0}^{\infty} z^{-l}\right)^n}{(-1)^n z^{-n}} = \frac{z^n}{(-1)^n}\left(\frac{1}{1-z^{-1}}\right)^{(n)} \tag{42}$$

where (n) denote nth-order derivative, we have

$$B^n(z) = (1-z^{-1})^{n+1}\frac{z^n}{(-1)^n}\left(\frac{1}{1-z^{-1}}\right)^{(n)}. \tag{43}$$

From this formula, we can also get the relation of z transforms of discrete sampling B-splines between different orders

$$B^n(z) = z^{-1}B^{n-1}(z) - \frac{z-1}{n}\frac{\partial}{\partial z}B^{n-1}(z) \tag{44}$$

or, alternatively in the space domain, we have the recursive relation shown in (45) at the bottom of the page.

Then through this recursive relation we could compute the z transforms of discrete B-splines of any orders and hence their

$$\begin{cases} b^n(1) = \frac{1}{n}b^{n-1}(1) \\ b^n(k) = \left(1 - \frac{k-1}{n}\right)b^{n-1}(k-1) + \frac{k}{n}b^{n-1}(k), & 2 \leq k \leq n-1 \\ b^n(n) = \frac{1}{n}b^{n-1}(n-1) \end{cases} \tag{45}$$

$$b^6(1)=\frac{1}{720},\quad b^6(2)=\frac{57}{720},\quad b^6(3)=\frac{302}{720},$$
$$b^6(4)=\frac{302}{720},\quad b^6(5)=\frac{57}{720},\quad b^6(6)=\frac{1}{720},$$
$$b^6(k)=0,\ \ k\neq 1,2,3,4,5,6 \tag{59}$$
$$B^7(z)=\frac{z^{-1}+120z^{-2}+1191z^{-3}+2416z^{-4}+1191z^{-5}+120z^{-6}+z^{-7}}{5040} \tag{60}$$

corresponding spatial responses starting from zeroth-order B-splines.

By the definition of B-splines (8), it is obvious that

$$B^0(z)=1 \tag{46}$$

or in the spatial domain, we have

$$b^0(k)=1,\quad k\in Z \tag{47}$$

then, through (44) and (45) we know

$$B^1(z)=\frac{(1-z^{-1})^2}{-1}z\left(\frac{1}{1-z^{-1}}\right)^{(\prime)}=z^{-1} \tag{48}$$

and in the spatial domain, we obtain that

$$b^1(1)=1,\quad b^1(k)=0,\ \ k\neq 1. \tag{49}$$

We write down $B^n(z)$ for higher orders and corresponding discrete filters, which are used for cubic spline approximations in this section

$$B^2(z)=\frac{z^{-1}+z^{-2}}{2} \tag{50}$$

and

$$b^2(1)=\frac{1}{2},\quad b^2(2)=\frac{1}{2},\quad b^2(k)=0,\ \ k\neq 1,2 \tag{51}$$
$$B^3(z)=\frac{z^{-1}+z+4}{6z^2} \tag{52}$$

and

$$b^3(1)=\frac{1}{6},\quad b^3(2)=\frac{4}{6},\quad b^3(3)=\frac{1}{6},$$
$$b^3(k)=0,\ \ k\neq 1,2,3 \tag{53}$$
$$B^4(z)=\frac{11+z+11z^{-1}+z^{-2}}{24z^2} \tag{54}$$

and

$$b^4(1)=\frac{1}{24},\quad b^4(2)=\frac{11}{24},\quad b^4(3)=\frac{11}{24},\quad b^4(4)=\frac{1}{24},$$
$$b^4(k)=0,\ \ k\neq 1,2,3,4 \tag{55}$$
$$B^5(z)=\frac{z^2+26z+66+26z^{-1}+z^{-2}}{120z^3} \tag{56}$$

and

$$b^5(1)=\frac{1}{120},\quad b^5(2)=\frac{26}{120},\quad b^5(3)=\frac{66}{120},$$
$$b^5(4)=\frac{26}{120},\quad b^5(5)=\frac{1}{120},\quad b^5(k)=0, k\neq 1,2,3,4,5 \tag{57}$$
$$B^6(z)=\frac{z^{-1}+57z^{-2}+302z^{-3}+302z^{-4}+57z^{-5}+z^{-6}}{720} \tag{58}$$

and as in (59) and (60) (shown at the top of the page) and

$$b^7(1)=\frac{1}{5040},\quad b^7(2)=\frac{120}{5040},\quad b^7(3)=\frac{1191}{5040},$$
$$b^7(4)=\frac{2416}{5040},\quad b^7(5)=\frac{1191}{5040},\quad b^7(6)=\frac{120}{5040},$$
$$b^7(7)=\frac{1}{5040},\quad b^7(k)=0,\ \ k\neq 1,2,3,4,5,6,7 \tag{61}$$

ACKNOWLEDGMENT

The authors would like to thank J. Huang.

REFERENCES

[1] A. A. Amini, R. W. Curwen, and J. C. Gore, "Snakes and splines for tracking nonrigid heart motion," in *Proc. Eur. Conf. Computer Vision*, Cambridge, U.K., Apr. 1996, pp. 251–261.

[2] A. A. Amini *et al.*, "Energy-minimizing deformable grids for tracking tagged MR cardiac images," in *Computers in Cardiology*. Durham, NC, Germany: Springer-Verlag, 1992, pp. 651–654.

[3] A. A. Amini, Y. Chen, R. Curwen, V. Mani, and J. Sun, "Coupled B-snake grids Coupled B-snake grids and constrained thin-plate splines for analysis of 2-D tissue deformations from tagged MRI," *IEEE Trans. Med. Imag.*, vol. 17, pp. 344–356, June 1998.

[4] A. A. Amini, Y. Chen, and D. Abendschein, "Comparison of landmark-based and curve-based thin plate warps for analysis of left ventricular motion from tagged MRI," in *Medical Image Computing and Computer Assisted Interventions*. Cambridge, U.K.: Univ. Cambridge Press, 1999.

[5] T. Arts, W. Hunter, A. Douglas, A. Muijtjens, and R. Reneman, "Description of the deformation of the left ventricle by a kinematic model," *J. Biomech.*, vol. 25, no. 10, pp. 1119–1127, 1992.

[6] L. Axel and L. Dougherty, "MR imaging of motion with spatial modulation of magnetization," *Radiology*, vol. 171, no. 3, pp. 841–845, 1989.

[7] A. Blake, R. Curwen, and A. Zisserman, "A framework for spatio-temporal control in the tracking of visual contours," *Int. J. Comput. Vis.*, vol. 11, no. 2, pp. 127–145, 1993.

[8] F. Bookstein, "Principal warps: Thin-plate splines and the decomposition of deformations," *IEEE Trans. Pattern Anal. Machine Intell.*, vol. 11, pp. 567–585, June 1989.

[9] T. Denney and J. Prince, "Reconstruction of 3-D left ventricular motion from planar tagged cardiac MR images: An estimation-theoretic approach," *IEEE Trans. Med. Imag.*, vol. 14, pp. 625–635, Dec. 1995.

[10] G. Golub and C. V. Loan, *Matrix Computations*, 3rd ed. Baltimore, MD: Johns Hopkins Univ. Press, 1996.

[11] S. Gupta and J. Prince, "On variable brightness optical flow for tagged MRI," in *Proc. Information Processing in Medical Imaging (IPMI)*, 1995, pp. 323–334.
[12] J. Huang, D. Abendschein, V. G. Davila-Roman, and A. Amini, "Spatio-temporal tracking of myocardial deformations with a 4-D B-spline model from tagged MRI," *IEEE Trans. Med. Imag.*, vol. 18, pp. 957–972, Oct. 1999.
[13] A. Klein, F. Lee, and A. Amini, "Quantitative coronary angiography with deformable spline models," *IEEE Trans. Med. Imag.*, vol. 16, pp. 468–482, Oct. 1997.
[14] L. L. Schumaker, *Spline functions: Basic Theory*. New York: Wiley, 1981.
[15] W. O'Dell, C. Moore, W. Hunter, E. Zerhouni, and E. McVeigh, "Three-dimensional myocardial deformations: Calculation with displacement field fitting to tagged MR images," *Radiology*, vol. 195, no. 3, pp. 829–835, 1995.
[16] J. Park, D. Metaxas, and L. Axel, "Volumetric deformable models with parameter functions: A new approach to the 3-D motion analysis of the LV from MRI-SPAMM," in *Proc. Int. Conf. Computer Vision*, 1995, pp. 700–705.
[17] P. Radeva, A. Amini, and J. Huang, "Deformable B-Solids and implicit snakes for 3-D localization and tracking of SPAMM MRI data," *Comput. Vis. Image Understanding*, vol. 66, no. 2, pp. 163–178, May 1997.
[18] N. Reichek, "Magnetic resonance imaging for assessment of myocardial function," *Magn. Reson. Quart.*, vol. 7, no. 4, pp. 255–274, 1991.
[19] M. Unser, A. Aldroubi, and M. Eden, "B-spline signal processing: Part 1 and Part 2," *IEEE Trans. Signal Processing*, vol. 41, pp. 821–847, Feb. 1993.
[20] G. Wahba, "Spline methods for observational data," in *Proc. SIAM CBMS-NSF*, Philadephia, PA, 1990.
[21] E. Waks, J. Prince, and A. Douglas, "Cardiac motion simulator for tagged MRI," in *Proc. Mathematical Methods in Biomedical Image Analysis*, 1996, pp. 182–191.
[22] Y.-P. Wang and S. L. Lee, "Scale-space derived from B-splines," *IEEE Trans. Pattern Anal. Machine Intell*, vol. 20, pp. 1040–1055, Oct. 1998.
[23] Y.-P. Wang, "Image representations using multiscale differiential operators," *IEEE Trans. Image Processing*, vol. 8, pp. 1757–1771, Dec. 1999.
[24] A. Young, D. Kraitchman, L. Dougherty, and L. Axel, "Tracking and finite element analysis of stripe deformation in magnetic resonance tagging," *IEEE Trans. Med. Imaging*, vol. 14, pp. 413–421, Sept. 1995.